An energetic evaluation of the response of the Walker circulation to warming

Margaret L. Duffy[1,2], **Paul A. O'Gorman**[2]

[1]National Center for Atmospheric Research, Boulder, CO
[2]Department of Earth, Atmospheric and Planetary Sciences, Massachusetts Institute of Technology, Cambridge, MA

Key Points:

- The atmosphere plays an important role in setting the large spread in the Walker circulation (WC) response to warming in coupled models
- Energetic analysis shows the WC response and its spread are strongly related to the response of the gross moist stability (GMS)
- The responses of the WC and GMS exhibit modest sensitivity to convective entrainment in an idealized general circulation model

Corresponding author: Margaret L. Duffy, `mlduffy@ucar.edu`

Abstract

The response of the Pacific Walker circulation (WC) to warming in both observations and simulations is uncertain. We diagnose contributions to the WC response in comprehensive and idealized general circulation model (GCM) simulations. We find that the spread in WC response is substantial across both the Coupled Model Intercomparison Project (CMIP6) and the Atmospheric Model Intercomparison Project (AMIP) models, implicating differences in atmospheric models in the spread in projected WC strength. Using a moist static energy (MSE) budget, we evaluate the contributions to changes in the WC strength related to changes in gross moist stability (GMS), horizontal MSE advection, radiation, and surface fluxes. We find that the multimodel mean WC weakening is mostly related to changes in GMS and radiation. Furthermore, different GMS responses can explain a substantial portion of the spread in WC responses. The GMS response is potentially sensitive to parameterized convective entrainment which can affect lapse rates and the depth of convection. We thus investigate the role of entrainment in setting the GMS response by varying the entrainment rate in an idealized GCM. The idealized GCM is run with a simplified Betts-Miller convection scheme, modified to represent entrainment. The weakening of the WC with warming in the idealized GCM is dampened when higher entrainment rates are used. However, the spread in GMS responses due to differing entrainment rates is much smaller than the spread in GMS responses across CMIP6 models. Therefore, further work is needed to understand the large spread in GMS responses across CMIP6 and AMIP models.

1 Introduction

The Pacific Walker circulation (WC) is an atmospheric zonal circulation over the equatorial Pacific Ocean. The WC transports energy from the West Pacific to the East Pacific (Trenberth & Stepaniak, 2003) in response to differing sea surface temperatures (SSTs) and net energy input to the atmosphere in the West and East Pacific. The WC is associated with a zonal surface pressure gradient over the Pacific Ocean, whose interannual variability comprises the Southern Oscillation. How the WC responds to a warming climate has been assessed using a combination of theory, observations, historical model trends, and model projections. Together, these lines of evidence give an unclear picture of the response of the WC to warming.

There are a number of proposed mechanisms for the response of the WC to warming, some of which suggest a weakening and some of which suggest a strengthening. Tropical convective mass fluxes must weaken overall with warming because increases in precipitation which are energetically constrained to lag increase in specific humidity which are set by the Clausius-Clapeyron relationship (Held & Soden, 2006). However, it is not clear that local changes in the WC must follow overall changes in convective mass fluxes (Merlis & Schneider, 2011). Knutson and Manabe (1995) found a weakening of the WC in projections despite an increase in precipitation in the ascent region. Increases in dry static stability, which are the result of changes in moist adiabatic lapse rate, are implicated in this weakening (Knutson & Manabe, 1995; Ma et al., 2012; Sohn et al., 2016). Further, differential increases in evaporative damping between the warm West Pacific and cool East Pacific weaken the SST gradient (Knutson & Manabe, 1995). Additionally, cloud masking, a direct CO_2 effect, contributes a weakening of the tropical circulation (Merlis, 2015).

In contrast, an ocean dynamical thermostat mechanism and changes in anthropogenic aerosols may contribute a strengthening of the zonal SST gradient with warming (Clement et al., 1996; Heede & Fedorov, 2021). The ocean dynamical thermostat mechanism, which was proposed using a highly idealized ocean model, strengthens the zonal SST gradient through (1) upwelling of relatively cool water in the equatorial East Pacific, thereby increasing the zonal SST gradient, and (2) increase in surface easterly winds further in-

crease this gradient (Clement et al., 1996). An analysis of coupled GCMs from CMIP3 found the upwelling portion of the mechanism to be operating but not the atmospheric portion of the mechanism because the surface easterly winds tend to weaken in the models, and the net effect is a slight weakening of the zonal SST gradient (DiNezio et al., 2009). Further, analysis of changes in historical CMIP6 simulations from 1950 to 2014 suggests a relative cooling of the equatorial East Pacific due to changes in aerosols, contributing an initial strengthening tendency of the WC (Heede & Fedorov, 2021).

Observational and reanalysis products going back only a few decades indicate a strengthening of the WC (Sohn et al., 2016), while observations over the past century indicate a weakening (Vecchi et al., 2006). This discrepancy may be explained by the large role of internal variability which means that long time periods are needed to evaluate trends in the WC (Vecchi et al., 2006). Coupled climate model trends over the historical period of observed WC strengthening are mixed, with some models indicating a weakening and others indicating a strengthening, though no model strengthens to the same extent as observations (Sohn et al., 2016). Projections of a warm 21st century climate almost unanimously indicate a WC weakening, but with substantial spread in the degree of weakening (Vecchi & Soden, 2007).

Here we seek to understand the spread in WC response across GCM projections through an energetic approach. We are motivated by the study of Wills et al. (2017) which used a moist static energy (MSE) budget to analyze the response of the WC to warming in simulations with an idealized GCM. Wills et al. (2017) found that the WC strength varied inversely with the gross moist stability (GMS) across a range of climates. GMS measures the efficiency of a circulation in exporting energy (Neelin & Held, 1987; Raymond et al., 2009). GMS has the advantage over the dry static stability, which has previously been used to explain changes in the WC (Knutson & Manabe, 1995; Sohn et al., 2016), that it can account for both dry adiabatic cooling and convective heating associated with ascent. For a given zonal gradient of net energetic input to the atmosphere, we expect an increase in GMS with warming to correspond to a weaker WC (Wills et al., 2017). In general, we expect the GMS to increase with warming owing predominantly to an increase in tropopause height (Chou et al., 2013). In the observed atmosphere and in more realistic simulations, we expect a more complicated relationship between GMS and WC responses than in the idealized simulations of Wills et al. (2017). Nonetheless, we also find an inverse relationship between WC response and changes in GMS in CMIP6 and AMIP models.

The close relationship we find between the responses of WC strength and GMS across CMIP6 and AMIP simulations warrants further investigation into the response of GMS to warming. We focus on the role of convective entrainment in setting the response of the WC and GMS. In general, entrainment is the process by which a cloud or buoyant plume mixes with the environment. Increasing entrainment affects GMS by (1) steepening the temperature lapse rate (Held et al., 2007; Singh & O'Gorman, 2013) and (2) increasing the top-heaviness of vertical velocity profiles (Singh & Neogi, 2022). However, it is difficult to represent entrainment in GCMs because it occurs on subgrid scales and is difficult to measure directly (Romps, 2010). Following Wills et al. (2017), we use an idealized GCM (Frierson et al., 2006; O'Gorman & Schneider, 2008) with a simplified Betts-Miller (SBM) convection scheme (Frierson, 2007) to study the response of the WC to warming. Here we modify the SBM scheme to represent entrainment so that we can evaluate the role of entrainment in the WC and GMS changes across climates.

This paper has two aims: (1) diagnose the contributions to the mean and spread of the WC response to warming in CMIP6 and AMIP simulations using an MSE budget, and (2) evaluate the influence of entrainment on WC strength and its response to warming in simulations with an idealized GCM. We address the first aim in Section 2 and the second aim in Section 3. We discuss and conclude in Section 4.

2 Response of WC to warming in CMIP6 and AMIP simulations

2.1 WC decomposition using GMS and the MSE budget

We diagnose the contributions to the response of the Walker circulation to warming across CMIP6 and AMIP models. We use monthly data of each variable and take the time average of calculated terms in a given climate before calculating the difference between warm and control climates. For the CMIP6 simulations, 'control climate' refers to the historical experiment for the years 1970-1999 and 'warm climate' refers to the SSP5-8.5 experiment for the years 2070-2099. For the AMIP simulations, 'control climate' refers to the 'amip' experiment for the years 1979-2014 and 'warm climate' refers to the 'amip-future4K' experiment for the years 1979-2014. The same ensemble member is used for both control and warm experiments. The imposed SST field of the 'amip-future4K' experiment is of a simulated warming, including a change in pattern. We use one model from each modeling center, matching the AMIP and CMIP6 models where possible. Some models were eventually excluded from the analysis for missing data or excessive spectral ringing. The models used here are shown in Table 1. Tropical-mean skin temperature warming from 20°S to 20°N is used to normalize throughout (i.e., to calculate rates of change in % K^{-1}).

We develop a framework for diagnosing contributions to changes in WC strength using the MSE budget. The WC strength is measured by -$\overline{\omega}_{w-e}$, where ω is vertical velocity in pressure coordinates, the overbar indicates a vertical average in pressure over the depth of the atmosphere, and $w-e$ denotes a horizontal average over a western Pacific box minus a horizontal average over an eastern Pacific box. Both boxes extend from 5°S to 5°N. The western Pacific box extends from 80°E to 160°E and the eastern Pacific box extends from 160°W to 80°W. The western Pacific box includes a small portion of the Indian ocean.

We difference the MSE budget in the time average between the western and eastern boxes to give

$$\left\langle \omega \frac{\partial h}{\partial p} \right\rangle_{w-e} \approx -\left\langle \mathbf{u} \cdot \nabla h \right\rangle_{w-e} + R_{w-e} + S_{w-e}, \tag{1}$$

where $\langle \cdot \rangle$ indicates a mass-weighted vertical integral, the subscript $w-e$ indicates the difference between western and eastern boxes, $\mathbf{u}$ are horizontal winds, R is the sum of net longwave and shortwave radiative fluxes into the atmosphere (including at both the surface and top of atmosphere), S is the sum of upward surface fluxes of latent and sensible heat, and $h = c_p T + gz + Lq$ is MSE where c_p is the heat capacity of dry air, T is temperature, g is acceleration due to gravity, z is height, L is latent heat of vaporization, and q is specific humidity. All four terms in Equation 1 are implicitly taken to be time averages in a given climate assuming a statistical steady state, and we are neglecting sub-monthly eddy terms which are expected to be small.

A definition of GMS appropriate for the WC is used here. The GMS is the ratio of vertical advection of MSE, differenced between the western and eastern boxes, to the WC strength and is given by

$$\text{GMS} \equiv -g \frac{\left\langle \omega \frac{\partial h}{\partial p} \right\rangle_{w-e}}{\overline{\omega}_{w-e}}. \tag{2}$$

We further introduce $\hat{\omega} = \frac{\omega}{\overline{\omega}_{w-e}}$ as the shape of the vertical-velocity profile to give the simple form

$$\text{GMS} = -g \left\langle \hat{\omega} \frac{\partial h}{\partial p} \right\rangle_{w-e}, \tag{3}$$

so that GMS can be thought of as depending on the shape of the vertical velocity profile and the MSE stratification, rather than directly on the WC strength. Our definition of GMS is similar to that of Wills et al. (2017) with two differences. First, instead of taking a zonal anomaly, we take the difference between the western and eastern Pacific boxes.

Second, we use a different definition of WC strength. Wills et al. (2017) defined the WC strength by the zonally-anomalous vertical velocity at the level of its maximum, ω^*_{max}. Instead, we use vertically averaged ω and the difference between the western and eastern Pacific boxes to give $\overline{\omega}_{w-e} = p_s^{-1} \int \omega_{w-e} dp$ where p_s is surface pressure.

In order to derive a diagnostic expression for WC strength from the MSE budget, we combine Equations 1 and 2 to give

$$-\overline{\omega}_{w-e} \approx g \frac{-\langle \mathbf{u} \cdot \nabla h \rangle_{w-e} + R_{w-e} + S_{w-e}}{\text{GMS}}. \tag{4}$$

Considering a perturbation due to climate change gives an expression for the fractional change in WC strength as a function of changes in GMS, horizontal MSE advection, surface heat fluxes, and radiation:

$$\delta\overline{\omega}_{w-e} \approx -\delta\text{GMS} - \frac{\Delta \langle \mathbf{u} \cdot \nabla h \rangle_{w-e}}{\left\langle \omega \frac{\partial h}{\partial p} \right\rangle_{w-e}} + \frac{\Delta R_{w-e}}{\left\langle \omega \frac{\partial h}{\partial p} \right\rangle_{w-e}} + \frac{\Delta S_{w-e}}{\left\langle \omega \frac{\partial h}{\partial p} \right\rangle_{w-e}}. \tag{5}$$

Here and throughout the paper, Δ indicates a response to warming, δ is the fractional response to warming given by $\delta X = \frac{\Delta X}{X}$ where X is the average between the control and warm climates. Note that $\left\langle \omega \frac{\partial h}{\partial p} \right\rangle_{w-e}$ is also evaluated as the average between the control and warm climates to increase accuracy. The terms on the RHS of Equation 5 are the contributions to the WC response from changes in GMS, horizontal advection, radiation, and surface heat fluxes, respectively. Equations 1,4, and 5 are approximations to the extent that there are errors due to, for example, finite differencing in calculating advection terms and neglect of sub-monthly eddy terms.

We further decompose the radiation contribution into a contribution from changes in WC strength and a contribution not related to changes in WC strength using a linear regression of radiation as a function of WC strength. The regression is taken across the 12 climatological monthly means for each model and climate and is given by

$$R_{w-e} \approx r_1 \overline{\omega}_{w-e} + R_0, \tag{6}$$

where r_1 and R_0 are regression coefficients. GMS and r_1 could be combined to form an effective GMS similar to that of Su and Neelin (2002), but here we find it more helpful to keep them separate given the different physical processes involved. Having fit r_1 and R_0 using the seasonal cycle, we now return to the average over all months in each climate and take the difference between climates to give

$$\Delta R_{w-e} \approx r_1 \Delta\overline{\omega}_{w-e} + \Delta r_1 \overline{\omega}_{w-e} + \Delta R_0. \tag{7}$$

The first term on the RHS is interpreted as the contribution to ΔR_{w-e} which is linked with changes in WC strength, and the last two terms on the RHS are interpreted as the contribution to ΔR_{w-e} which is not linked with changes in WC strength.

2.2 WC response and decomposition in CMIP6

In order to diagnose contributions to changes in WC strength in coupled GCMs, we apply the decomposition given by Equation 5 to each CMIP6 model. Figure 1a shows the decomposition in the multimodel mean and the spread across models, and Figure S1 shows the decomposition in individual CMIP6 models. We find that the WC weakens in all models, with a weakening ranging from a 6% K^{-1} to 20% K^{-1}. The multimodel mean weakening of 12% K^{-1} is greater than the 5 to 10% K^{-1} estimated by Vecchi and Soden (2007) using changes in ω at 500 hPa and this is partly because we normalize by changes in tropical mean SST warming rather than global-mean surface warming as in Vecchi and Soden (2007).

Looking at Figures 1a and S1, we notice that the relative roles of each mechanism in setting the WC response can vary substantially across models, but a few important commonalities emerge. The response of GMS contributes a weakening of the WC in all models. That is, GMS increases with warming in all models, consistent with Chou et al. (2013). The contribution from changes in GMS ranges from a weakening of 4 to 18% K^{-1}. The total radiation contribution also contributes a weakening in all models, ranging from a weakening of 1% K^{-1} to 18% K^{-1}. The total radiation contribution is well approximated by the sum of the WC-linked and not WC-linked potions, with the WC-linked portion dominating in the multimodel mean (Figure 1c). Thus, the weakening contribution from radiation in the multimodel mean is largely due to an amplifying feedback of radiation on WC response (cf. Peters and Bretherton (2005)).

2.3 WC response and decomposition in AMIP

In order to isolate the atmospheric contribution to the spread in WC response, we analyze the response of the WC in AMIP simulations using the 'amip' and 'amip-future4K' experiments. Recall that all of the 'amip' experiments have the same imposed SST distribution as one another and all of the 'amip-future4K' experiments have the same imposed SST distribution as one another.

As we did with the CMIP6 models, we apply the decomposition given by Equation 5 to each AMIP model. Figure 1b shows the decomposition in the multimodel mean and the spread across models, and Figure S3 shows the decomposition in individual AMIP models. Even with the same SST response across models, there is spread in the weakening response of the WC from 8 to 20% K^{-1} which is similar to the range for the CMIP6 simulations which have interactive oceans. However, the spread due to changes in surface heat fluxes is larger in AMIP than in CMIP6, which may be the result of artificially imposing SSTs. Therefore, while the substantial spread in WC response across AMIP models does not rule out some role for the ocean in setting the spread in CMIP6, it does suggest an important role of the atmosphere in setting the spread in CMIP6 response. Similar to the CMIP6 simulations, the WC response is dominated by changes in GMS and radiation; both contribute a weakening in all AMIP simulations. The contribution from changes in GMS range from a weakening of 6 to 19% K^{-1}, while the contribution from changes in radiation range from a weakening of 3 to 8% K^{-1}. Further, the radiation contribution is dominated by changes in the WC-linked portion in the multimodel mean (Figure 1d).

Given the large contribution from the increase in GMS in both the CMIP6 and AMIP simulations, we further investigate the contribution of changes in GMS to WC response.

2.4 Relationship between WC and GMS responses

We expect GMS to vary inversely with WC strength because a larger increase in GMS indicates a weaker response of the atmospheric circulation for a given energetic forcing. Figure 2 shows that the relationship between responses of WC strength and GMS in CMIP6 and AMIP models are consistent with this expectation: the WC weakens and GMS increases in all models, with a tendency for greater weakening of the WC with a greater increase in GMS. The correlation coefficient is -0.71 across the CMIP6 models and -0.91 across the AMIP models. Wills et al. (2017) showed a similar inverse relationship between WC strength and GMS in idealized GCM simulations. The strong anticorrelation between responses of WC strength and GMS indicates that the WC-GMS relationship holds in more complex simulations and warrants further investigation into the response of GMS to warming.

Figure 2 also shows the standard error of the WC response for each model. We calculate the standard error of the numerator, $\Delta\bar{\omega}_{w-e}$, by assuming it is independent be-

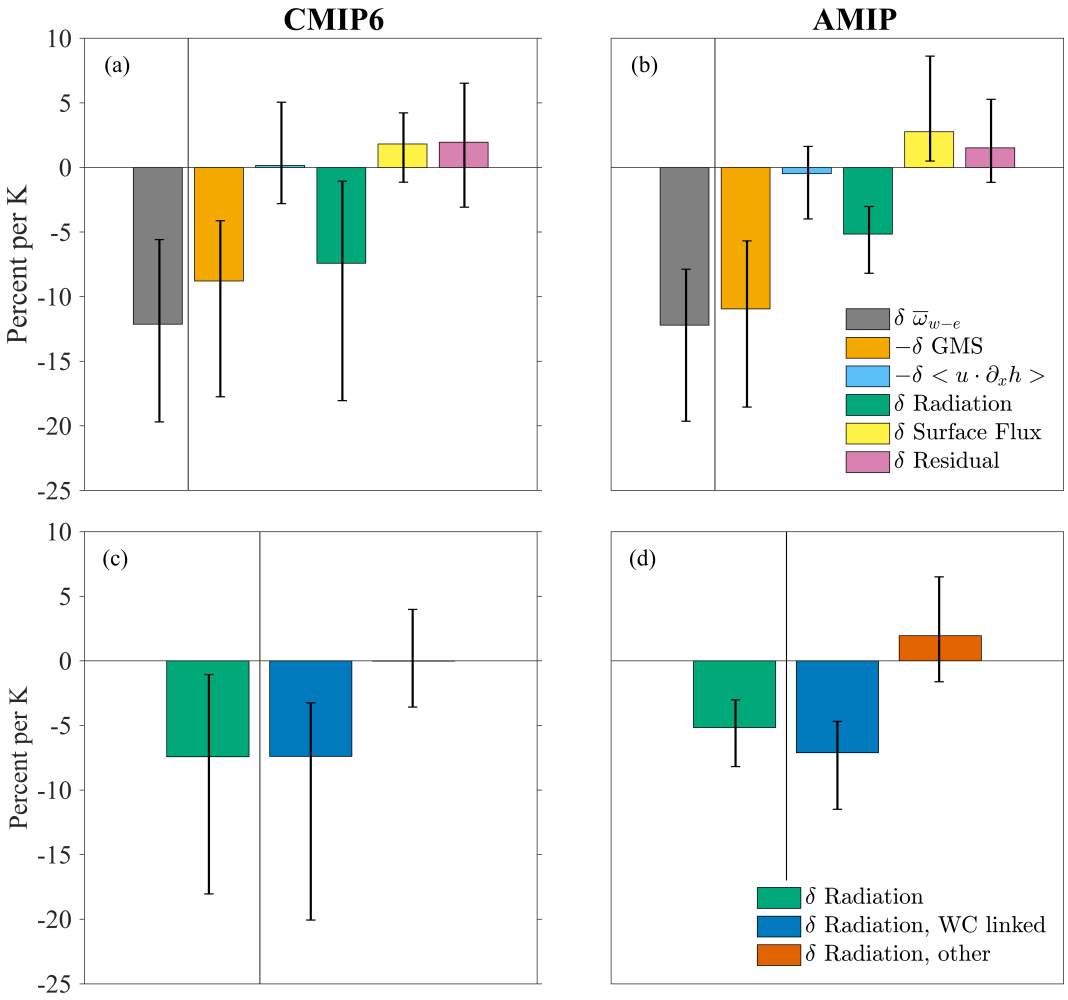

Figure 1. Contributions to multimodel mean response of WC to warming in (a) CMIP6 and (b) AMIP simulations. WC response (gray) is the sum of the contributions from each term on the RHS of Equation 5. The radiation contribution in (c) CMIP6 and (d) AMIP is decomposed into the portion that is linked to WC strength (darl blue) and the portion that is not linked with WC strength (dark orange). The radiation decomposition is performed using the seasonal cycle and Equation 7. The whiskers cover the spread across individual models.

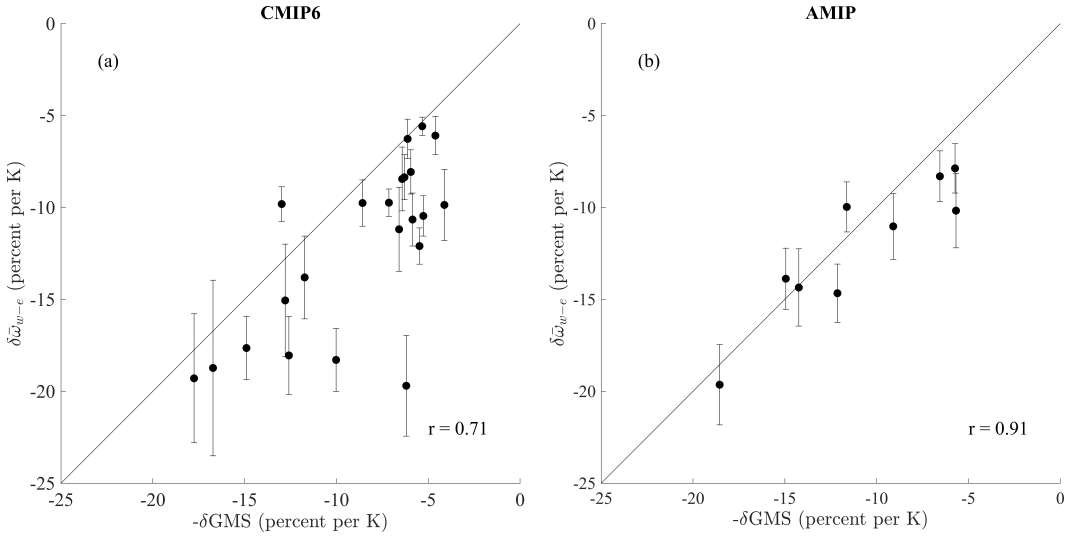

Figure 2. Relationship between responses of GMS and WC strength for (a) CMIP6 and (b) AMIP simulations. The error bars indicate the standard error of the WC response calculated as described in section 2.4. The one-to-one line is also shown.

tween different years and climates. We then normalize by $\bar{\omega}_{w-e}$ and multiply by $100/\Delta T_s$ so that the standard error has the same units as the plotted value. The standard errors are sufficiently small that we can be sure that the intermodel spread in WC response is not just due to unforced variability.

2.5 GMS decomposition

In order to better understand the response of GMS to warming in CMIP6 and AMIP models, we decompose the GMS response into contributions due to changes in vertical velocity and MSE profiles. Looking at Equation 3, the fractional change in GMS with warming has contributions from changes in the shape of the vertical velocity profile $\hat{\omega}$ and changes in the MSE (h) profile through $\partial h/\partial p$ as follows:

$$\delta\text{GMS} \approx \frac{\left\langle \Delta\hat{\omega}\frac{\partial h}{\partial p}\right\rangle_{w-e}}{\left\langle \hat{\omega}\frac{\partial h}{\partial p}\right\rangle_{w-e}} + \frac{\left\langle \hat{\omega}\Delta\frac{\partial h}{\partial p}\right\rangle_{w-e}}{\left\langle \hat{\omega}\frac{\partial h}{\partial p}\right\rangle_{w-e}}. \tag{8}$$

There is a small residual because monthly climatologies of $\hat{\omega}$ and $\partial h/\partial p$ are used in calculating the numerator. The results are shown for the multimodel means in Figure 3, for each CMIP6 model in Figure S2, and for each AMIP model in Figure S4. The $\hat{\omega}$ contribution is positive and considerably larger in magnitude than the h profile contribution for both CMIP6 and AMIP The positive contribution from changes in $\hat{\omega}$ is consistent with the increase in GMS from increasing tropopause height and an associated upward shift of $\hat{\omega}$ (Singh & O'Gorman, 2012; Chou et al., 2013; Wills et al., 2017).

Using the definition of $h = c_pT + gz + Lq$, the h profile contribution can be linearly decomposed into contributions from changes in temperature (T), geopotential height (z) and specific humidity (q). Further, the changes in specific humidity can be decomposed into its contributions from changes in saturation specific humidity (q_{sat}) and relative humidity (RH), according to $\Delta q \approx \Delta\text{RH}\, q_{sat} + \text{RH}\,\Delta q_{sat}$, where again there is a small residual since climatologies of each term are used. Figures 3, S2, and S4 show that changes in h profile tend to have small net contributions to changes in GMS, but this is the result of compensation between strong positive contributions from changes in T

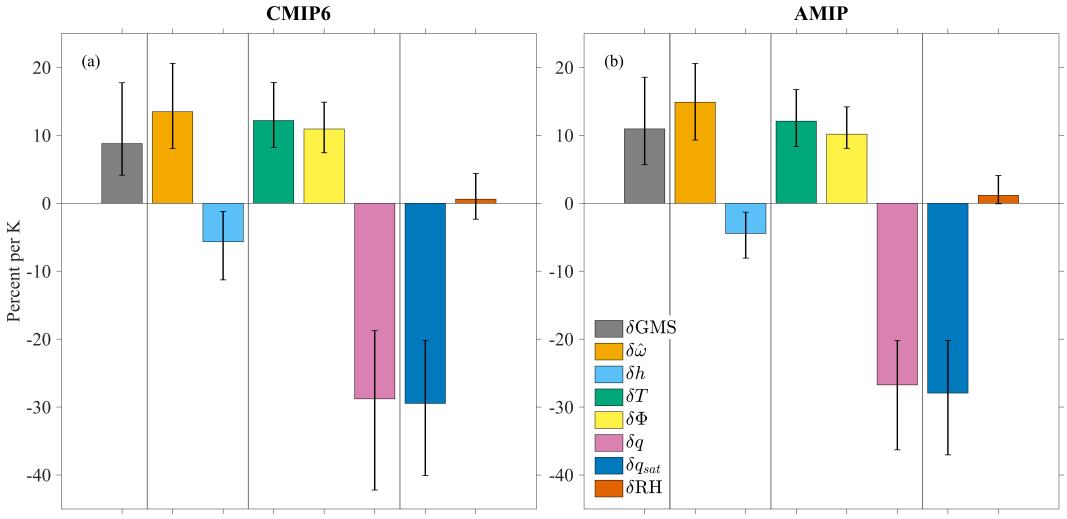

Figure 3. Contributions to the multimodel mean response of GMS to warming in (a) CMIP6 and (b) AMIP simulations. The response of GMS to warming (gray) is decomposed into contributions from changes in shape of vertical velocity profile (light orange) and changes in MSE (light blue) as in Equation 8. The MSE contribution is further decomposed into contributions from changes in temperature (green), geopotential height (yellow), and humidity (pink). The humidity contribution is further decomposed into contributions from changes in saturation specific humidity (dark blue) and relative humidity (dark orange). The whiskers cover the spread across individual models.

and Φ and a strong negative contribution from changes in specific humidity. The contribution from changes in specific humidity, which acts to decrease the GMS, is mostly the result of changes in saturation specific humidity. Note that our contributions from changes in T, z, and q assume constant $\hat{\omega}$, and thus our contributions differ from the contributions found in Wills et al. (2017) in which the increase in tropopause height was included.

Figure 3 shows that intermodel spread in changes in both the MSE profile and the shape of the vertical velocity profile contribute to the intermodel spread in the GMS response. We next investigate the role of convective entrainment in the GMS response given that it can affect both these factors.

3 The role of entrainment in setting GMS and WC strength in idealized GCM simulations

3.1 Why consider entrainment?

In order to further evaluate the spread in WC strength response, we study the role of entrainment in setting the WC strength and its response to warming in an idealized GCM. Entrainment is a parameterized process which is difficult to quantify in observations. However, entrainment can have a substantial effect on the climate, especially in the tropics (Singh & O'Gorman, 2013; Miyawaki et al., 2020). Entrainment affects the temperature lapse rate: a higher entrainment rate tends to steepen the temperature lapse rate in the lower and mid troposphere in GCM simulations (Held et al., 2007; Keil et al., 2021). Variations in temperature lapse rate with entrainment will also affect specific humidity, and both the temperature and humidity profiles influence the MSE profile, a key portion of the GMS. Further, entrainment can increase the top-heaviness of vertical ve-

locity profiles (Singh & Neogi, 2022) which again strongly influences the GMS (Inoue et al., 2021).

3.2 Idealized GCM simulations

Idealized simulations of the Walker circulation are run using an idealized moist atmospheric GCM based on the GFDL spectral dynamical core following Frierson et al. (2006) with details as in O'Gorman and Schneider (2008). The idealized GCM lacks land, a seasonal cycle, and cloud and water-vapor radiative feedbacks. The lower boundary is a thermodynamic mixed-layer ocean with a depth of 1 m. There is a zonal-mean Q flux with a maximum magnitude of 30 W m^2 and a latitudinal width parameter of 16° following Equation 1 of Merlis and Schneider (2011). Through missing a cosine latitude factor, this zonal-mean Q flux formulation induces a small global-mean sink of energy (Merlis et al., 2013) which is not expected to strongly affect the results presented here.

Following Wills et al. (2017), the WC is driven by a zonally anomalous component of the Q flux with an elliptic convergent region in the 'western' hemisphere (leading to atmospheric ascent) and an equal and opposite divergent region (leading to atmospheric descent) in the 'eastern' hemisphere, both centered on the equator. The zonally anomalous Q flux, Q^*, has the form

$$Q^* = Q_1 \exp\left[-\frac{(\lambda-\lambda_W)^2}{2\sigma_\lambda^2} - \frac{\phi^2}{2\sigma_\phi^2}\right] - Q_1 \exp\left[-\frac{(\lambda-\lambda_E)^2}{2\sigma_\lambda^2} - \frac{\phi^2}{2\sigma_\phi^2}\right], \tag{9}$$

where λ is longitude, ϕ is latitude, $Q_1 = 50$ W m^{-2} is the amplitude of the zonally anomalous Q flux, $\lambda_E = 270°$ is the longitude of the center of the descent region, $\lambda_W = 90°$ is the longitude of the center of the ascent region, $\sigma_\lambda = 12.5°$ is proportional to the zonal extent of the anomaly, and $\sigma_\phi = 8°$ is proportional to the meridional extent of the anomaly. The sign of the zonally anomalous Q flux is modified from Wills et al. (2017) such that positive indicates a flux from ocean to atmosphere. The imposed zonally anomalous Q flux is plotted in Figure S5.

The idealized simulations are spun up for four years, and the analysis is performed on the following eight years of simulation output. The convection scheme is a modification of the simplified Betts-Miller (SBM) convection scheme of Frierson (2007), which relaxes temperature profiles to a moist adiabat and relative humidity to 70% in convecting regions. Here, we modify the SBM scheme by introducing a non-dimensional entrainment parameter $\hat{\epsilon}$ such that the convection scheme relaxes to the temperature profile of an *entraining* plume when $\hat{\epsilon} > 0$. Our entraining SBM scheme reduces to the SBM convection scheme when $\hat{\epsilon} = 0$. Details about the modification to represent entrainment are given in Appendix A.

The longwave optical depth distribution is specified as a function of latitude and pressure and then scaled by a factor α (O'Gorman & Schneider, 2008). Two climates are simulated: a control climate with a default longwave optical depth ($\alpha = 1$) and a warm climate with doubled longwave optical depth ($\alpha = 2$). From the control to the warm climate there is a large warming with a global-mean SST increase of 11.2K and a tropical-mean (20°S to 20°N) SST increase of 9.1K in the simulations without entrainment.The ocean Q flux is held constant as the climate warms. We run the idealized model for simulations for a control climate and a warm climate with four values of the entrainment parameter $\hat{\epsilon}$, for a total of eight simulations. The four values of $\hat{\epsilon}$ are 0 (no entrainment), 0.125, 0.25, and 0.5.

3.3 Spread in MSE and $\hat{\omega}$ profiles

Before evaluating responses of WC strength and GMS to warming across entrainment rates in the idealized GCM, it is useful to examine the $\hat{\omega}$ and MSE profiles and their

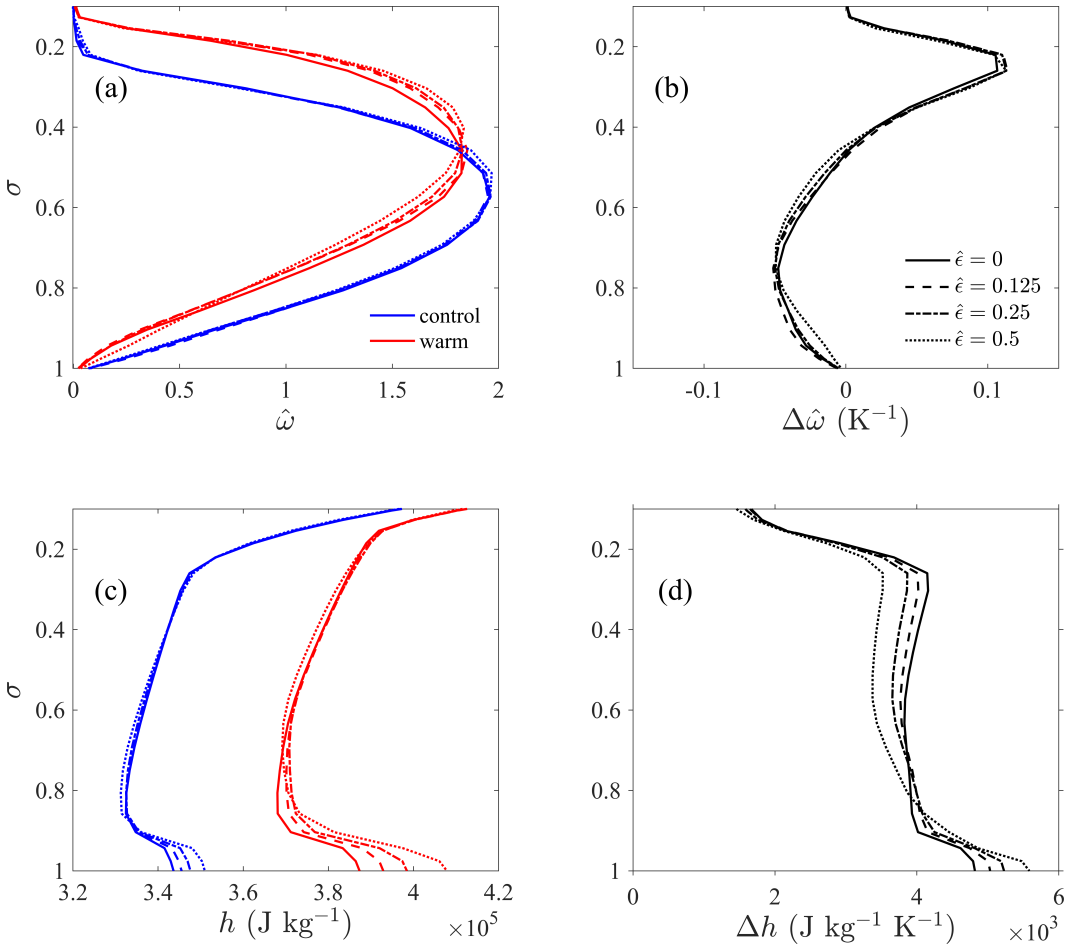

Figure 4. Profiles of (a) $\hat{\omega}$ and (c) MSE for various entrainment rates in the idealized GCM simulations. Responses of (b) $\hat{\omega}$ and (d) MSE profiles to warming. All profiles are averaged over the ascent region of the WC (see text for details).

responses to warming (Figure 4) since these affect the GMS response. For the idealized GCM, profiles are averaged over the boundary of the elliptic ascent region, consistent with the upcoming GMS analysis, with the boundary defined by the 10 W m^{-2} contours of Q flux which can be seen in Figure S5. Response profiles are normalized by tropical-mean SST warming. Overall Figure 4 shows that entrainment has a bigger effect in the warmer climate than in the control climate. The greater sensitivity to entrainment in a warmer climate is because entrainment in the convection scheme acts on the difference between the MSE of the environment and that of saturated rising air, and this difference is larger in the warm climate. Figures 4a,b reveal that $\hat{\omega}$ profiles have a tendency to shift upward with warming, and this upward shift is enhanced by convective entrainment. This enhancement in $\Delta\hat{\omega}$ is broadly consistent with Singh and Neogi (2022), who found that entrainment tends to make vertical velocity profiles more top heavy. Figures 4c,d reveal that MSE increases with warming, and that increases in entrainment have a tendency to steepen the MSE lapse rate, especially in the lower troposphere, and that this steepening is greater in the warmer climate.

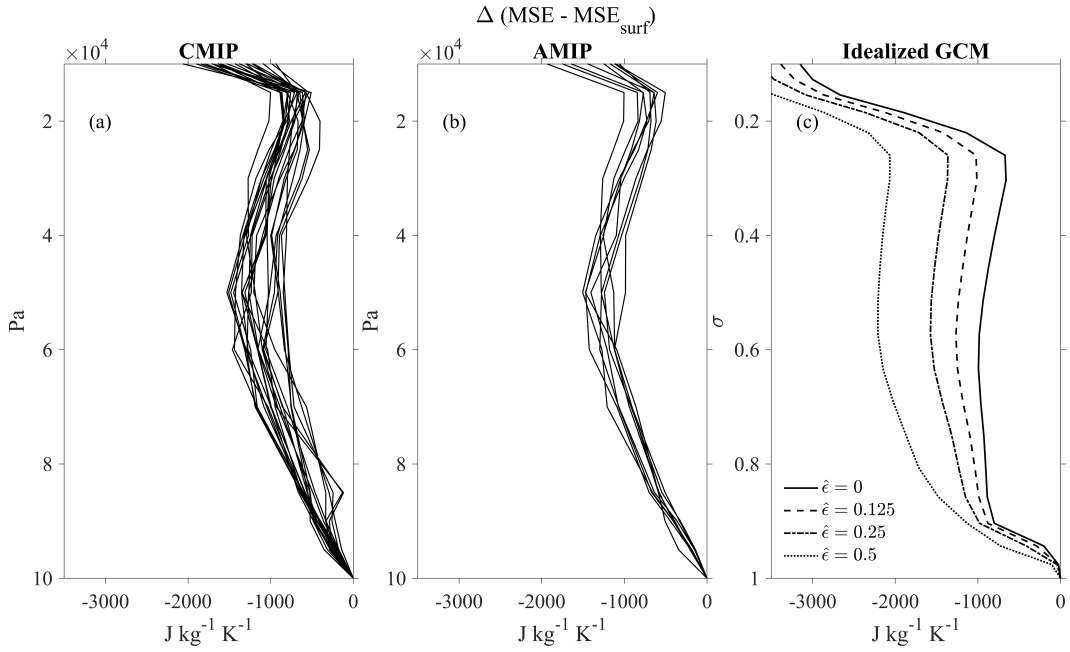

Figure 5. Response of MSE profiles to warming (a) across models in CMIP6, (b) across models in AMIP, and (c) across entrainment rates in the idealized GCM. Surface MSE responses for each profile is subtracted so that all profiles go through zero at the surface, and the profiles are normalized by the tropical-mean SST response. CMIP and AMIP profiles are in pressure coordinates and idealized profiles are in sigma coordinates. All results are averaged over the ascent region of the WC (see text for details).

3.4 Comparison of MSE and $\hat{\omega}$ profile responses in idealized GCM with CMIP6 and AMIP

We next compare the MSE and $\hat{\omega}$ profiles from the idealized GCM simulations to MSE and $\hat{\omega}$ profiles from CMIP6 and AMIP models. For the CMIP6 and AMIP models, profiles are averaged over the area of the western Pacific box. Figure 5 compares the response of MSE profiles to warming in CMIP6 models, AMIP models, and across entrainment rates in the idealized GCM. The response of surface MSE is subtracted from each profile since it is the vertical gradient of MSE which affects GMS. Figure 6 compares the response of $\hat{\omega}$ profiles to warming in CMIP6 models, AMIP models, and across entrainment rates in the idealized GCM.

We find that the spread in MSE profile response across entrainment rates in the idealized GCM is broadly similar to the spread in MSE profile response across CMIP6 and AMIP models. However, in the upper troposphere, MSE profile responses have greater spread across entrainment rates than across the CMIP6 and AMIP simulations. We hypothesize that this is because the convection scheme used in the idealized simulation represents a single plume instead of a sprectrum of plumes. We further find that the spread in $\hat{\omega}$ profile response across entrainment rates in the idealized simulations is very small as compared to the spread in CMIP6 and AMIP simulations. Thus we expect $\hat{\omega}$ changes to play a much bigger role for the spread in GMS and WC response in CMIP6 and AMIP compared to the variation across entrainment rates in the idealized GCM simulations.

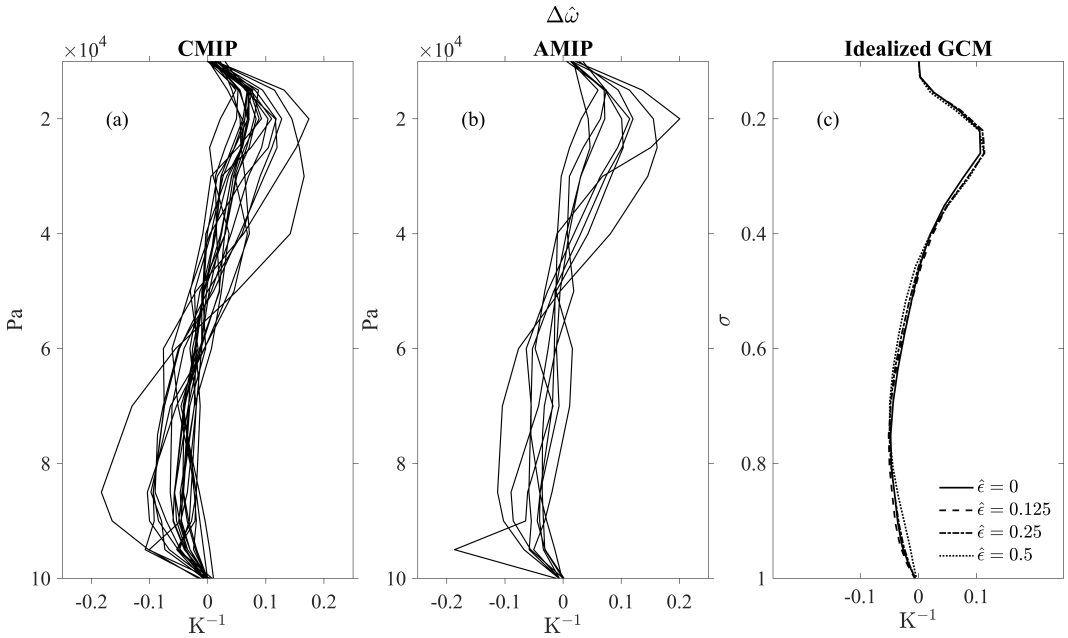

Figure 6. Response of $\hat{\omega}$ profiles to warming (a) across models in CMIP6, (b) across models in AMIP, and (c) across entrainment rates in the idealized GCM. The profiles are normalized by the tropical-mean SST response. CMIP and AMIP profiles are in pressure coordinates and idealized profiles are in sigma coordinates. All results are averaged over the ascent region of the WC (see text for details).

3.5 Sensitivity of WC strength to warming and entrainment in idealized simulations

The WC strength is defined as the negative of the average value of ω in the ascent region minus the average value of ω over the descent region. Further, we estimate the uncertainty in WC strength by using the WC strength in each of the eight simulated years to calculate the standard error for the eight-year average. The WC strength and its uncertainty are plotted in Figure 7a for each of the idealized GCM simulations. In general, the WC is weaker in the warm climate than in the control climate, consistent with the CMIP6 and AMIP simulations. WC strength increases with increasing entrainment in both climates, but the sensitivity to entrainment is greater in the warm climate. As a result, the WC weakens with warming more at lower entrainment rates than it does at higher entrainment rates. While entrainment does affect the response of the WC to warming, the spread due to variations in entrainment of 1.6% K^{-1} (Figure 8) is not as large as the spread due to differences across models in CMIP6 (14% K^{-1}) or AMIP (12% K^{-1}). Figures 5 and 6 suggest that this is because variations in entrainment only capture the size of the spread in MSE profile response, but not the size of the spread in $\hat{\omega}$ response. Further, this may be partly because radiative feedbacks are not as fully represented in the idealized model as they are in the CMIP6 and AMIP models, and our analysis in Sections 2.2 and 2.3 suggests that they have an amplifying effect on the WC response.

3.6 GMS in idealized simulations

From Wills et al. (2017), the Walker circulation strength varies inversely with the zonally-anomalous GMS in this idealized GCM when entrainment is set to zero. Here we determine whether this relationship between WC strength and GMS responses holds

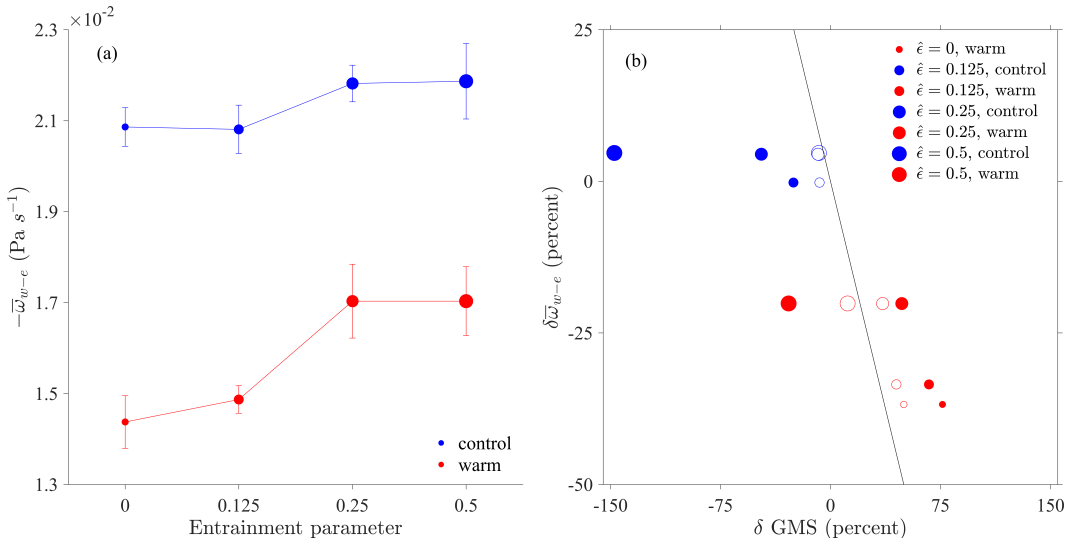

Figure 7. (a) WC strength versus entrainment for a control climate with default longwave optical depth (blue) and a warm climate with double longwave optical depth (red) in the idealized GCM simulations. Error bars show the standard error. (b) Relationship between GMS response and WC response in the idealized GCM simulations to warming and changes in entrainment. Delta indicates the fractional change from the reference case of the control climate ($\alpha = 1$) with zero entrainment ($\hat{\epsilon} = 0$). Filled circles indicate GMS response and open circles indicate boundary GMS response. Black line is a reference line with slope of -1. Blue symbols indicate that the perturbed climate is a control climate and red symbols indicate that the perturbed climate is a warm climate.

with variations in entrainment. Looking at Equation 1, we notice that in the idealized simulations the sum of changes in R_{w-e} and S_{w-e} is very small because the Q flux at the surface is fixed and changes in radiation are very nearly zonally uniform because the simulations do not have cloud-radiative effects or water vapor-radiative feedback. Therefore, the radiative and surface flux terms vanish from Equations 1 and 5 when applied to the idealized simulations. Consequently, in the idealized simulations, Equation 5 reduces to

$$\delta\overline{\omega}_{w-e} \simeq -\delta\text{GMS} - \frac{\Delta \left\langle \mathbf{u} \cdot \nabla h \right\rangle_{w-e}}{\left\langle \omega \frac{\partial h}{\partial p} \right\rangle_{w-e}}, \tag{10}$$

where δ is a fractional response and Δ is a difference between simulations in response to warming or changes in entrainment parameter. Equation 10 is an excellent approximation, and thus there is an inverse relationship between WC strength and GMS if changes in the horizontal MSE advection term are small.

To evaluate the role of horizontal MSE advection, we compare changes in WC strength and GMS. Figure 7b shows that GMS response does not have the expected inverse relationship with WC response (although this does hold approximately for the zero entrainment case that was also considered by Wills et al. (2017)), indicating that changes in horizontal advection terms are important in Equation 10. This is problematic because although we have some understanding of how entrainment affects the vertical MSE advection term through MSE and vertical velocity profiles, we do not have a similar understanding for horizontal MSE advection. In order to reduce the role of horizontal advection in our analysis, we define a new GMS appropriate for the WC in our idealized simulations called the "boundary GMS."

The boundary GMS is defined using MSE averaged over the *boundaries* of the WC ascent and descent regions which are defined in our idealized simulations based on contours of the zonally anomalous Q flux (Q^*). Between the surface and top of atmosphere, the Q^* contours create an elliptic cylinder for each region. We define h_b as the average value of h around the elliptic contour at each level and each time, so that h_b does not vary in latitude or longitude. The boundary GMS is then defined as

$$\mathrm{GMS}_b = -g\frac{\left\langle \omega \frac{\partial h_b}{\partial p} \right\rangle_{w-e}}{\overline{\omega}_{w-e}}. \tag{11}$$

To see why the boundary GMS is helpful, we decompose h at a given vertical level as the sum of h_b and a residual, h' such that $h = h_b + h'$. Considering the ascent region, the advection terms can now be written

$$\left\langle \omega \frac{\partial h}{\partial p} \right\rangle_w + \langle \mathbf{u} \cdot \nabla h \rangle_w = \left\langle \omega \frac{\partial h_b}{\partial p} \right\rangle_w + \left\langle \omega \frac{\partial h'}{\partial p} \right\rangle_w + \langle \mathbf{u} \cdot \nabla h' \rangle_w \,, \tag{12}$$

where we have used that h_b does not vary horizontally. A similar result holds for the descent region. In order for $\left\langle \omega \frac{\partial h_b}{\partial p} \right\rangle_w$ to dominate the right-hand side, we need h' advection , $\left\langle \omega \frac{\partial h'}{\partial p} \right\rangle_w + \langle \mathbf{u} \cdot \nabla h' \rangle_w = \langle \nabla_{3\mathrm{d}} \cdot (\mathbf{u}_{3\mathrm{d}} h') \rangle_w$, to be negligible. By the divergence theorem, this will be the case if h' is close to zero on the boundary, meaning that the h contours align with the -10 and 10 W m^{-2} surface Q^* contours. If this is approximately the case, then Equation 12 and the equivalent for the descent regions gives that

$$\left\langle \omega \frac{\partial h}{\partial p} \right\rangle_{w-e} + \langle \mathbf{u} \cdot \nabla h \rangle_{w-e} \simeq \left\langle \omega \frac{\partial h_b}{\partial p} \right\rangle_{w-e}. \tag{13}$$

Repeating the derivation of Equation 10 but using GMS_b gives that

$$\delta\overline{\omega}_{w-e} \simeq -\delta \mathrm{GMS}_b. \tag{14}$$

Looking at Figure 7b, we can see that the relationship between WC response and boundary GMS response is much closer to the slope -1 line than the relationship between WC response and GMS. The extent to which the WC and boundary GMS responses depart from the slope -1 line is due almost entirely to the neglect of h' advection. Still, the boundary GMS is a better metric than GMS for understanding the WC response across entrainment rates and climates in the idealized GCM. By contrast, it was sufficient to use the usual GMS in the analysis of the CMIP6 and AMIP simulations. Horizontal MSE advection does provide a contribution in the CMIP6 and AMIP simulations, but the multimodel mean of this contribution is close to zero and the model spread is not as big as the spread in the GMS contribution (Figures 1a,b). The lesser role for the horizontal advection term in the CMIP6 and AMIP simulations may be because of differences in the structure of the WC (e.g., due to the presence of topography) or because the range of entrainment parameters is not as wide as in the idealized GCM.

3.7 Boundary GMS response to warming and decomposition

Finally, we evaluate the response of boundary GMS to warming and compare it to the response of the WC. Looking at Figure 8, we find that the responses of boundary GMS and WC strength are of opposite sign, consistent with the inverse relationship found in Wills et al. (2017) and in the CMIP6 and AMIP models in Section 2 (although those results used GMS rather than boundary GMS). Further, both the weakening of the WC and the increase in boundary GMS with warming dampen with increasing entrainment rate. However, the decreases in WC strength are mostly smaller than the increases in

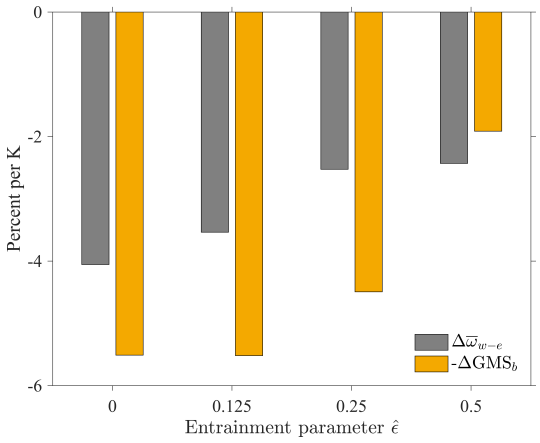

Figure 8. Response of WC strength (gray) to warming compared with minus the response of boundary GMS (orange) in idealized GCM simulations with varying entrainment rates.

boundary GMS, and this reflects that the boundary GMS does not fully account for contributions from changes in the horizontal MSE advection.

We decompose the response of boundary GMS to warming in the idealized simulation as was done in Section 2.5 but here replacing GMS with boundary GMS in Equation 8. Similar to the CMIP6 and AMIP results, the $\Delta\hat{\omega}$ contribution is positive and larger in magnitude than the negative Δh contribution (Figure 9). The Δh contribution is again the result of compensation between positive contributions due to temperature and geopotential height changes and a negative contribution from humidity changes. Again, the contribution from changes in humidity is dominated by changes in saturation specific humidity.

As the entrainment rate is increased, the increase in GMS with warming becomes weaker. This is mostly related to the Δh contribution becoming more negative, but it is partially compensated for by the $\Delta\hat{\omega}$ contribution becoming more positive. The more negative changes in Δh are as expected given that entrainment makes the atmosphere less stable and has a greater effect in the warmer climate than the control climate (Singh & O'Gorman, 2013). Looking at Figures 4a,b, since entrainment has more of an effect on $\hat{\omega}$ in the warmer climate, increasing the entrainment rate will also make the $\Delta\hat{\omega}$ contribution more positive. Further, changes in climatological MSE lapse rate can have an effect on the $\Delta\hat{\omega}$ contribution. Thus increasing entrainment does dampen the increase in GMS with warming as was expected initially, but there is less of an effect than would occur if only changes in h were considered.

Figure 9 shows that changes in specific humidity are the main reason that the Δh contribution becomes more negative as the entrainment rate increase, while the contribution from changes in temperature does not vary noticeably across entrainment rates. The greater contribution from changes in specific humidity with increasing entrainment is consistent with temperature lapse rates steepenings with incrasing entrainment, and more so in a warmer climate (Held et al., 2007; Singh & O'Gorman, 2013). But why do changes in lapse rates with increasing entrainment not affect the temperature contribution? It appears that entrainment also affects the control-climate GMS and Figure 9 shows the fractional response to warming. If instead absolute changes in GMS with warming are considered (Figure S6), the temperature contribution does become more negative as the entrainment rate is increased as expected.

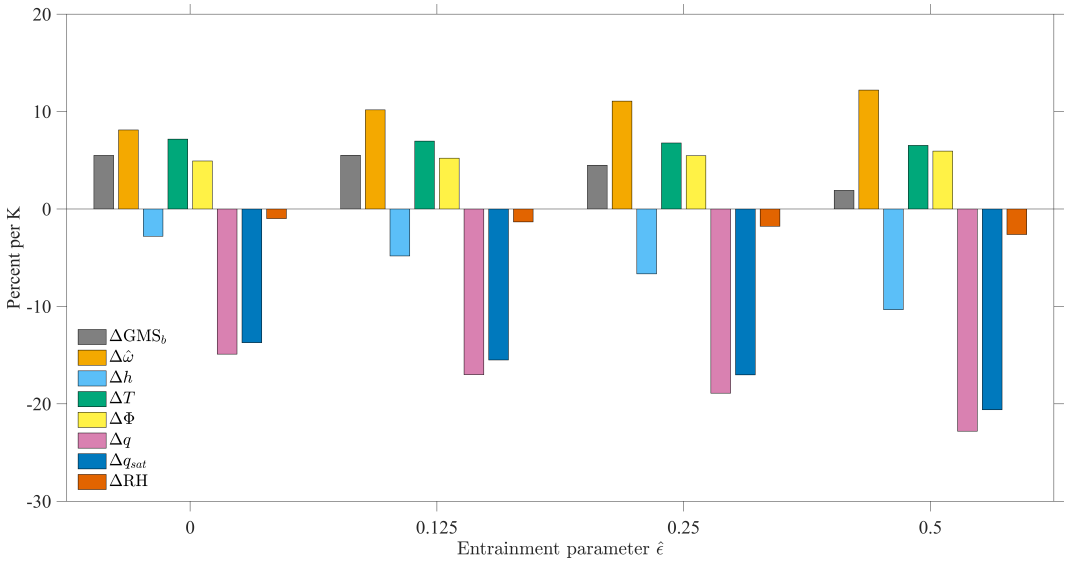

Figure 9. Same as Figure 3 but for idealized GCM simulations with varying entrainment rates and using the boundary GMS instead of GMS.

4 Conclusions

We have evaluated the response of the Walker circulation to warming in comprehensive and idealized GCM simulations using an energetic perspective, with an emphasis on the spread in the response across GCM projections. The gross moist stability (GMS) emerges as a key factor, consistent with the heuristic idea that for a given energy transport, a higher GMS is associated with a weaker circulation.

In an MSE budget analysis of WC strength in CMIP6 and AMIP simulations, a weakening of the WC is related primarily to increases in GMS and secondarily to changes in radiation. Changes in horizontal MSE advection and surface latent and sensible fluxes play a smaller role. We find a large spread in WC response to warming across CMIP6 models, with GMS response anticorrelated with WC response. The spread of WC response in the AMIP models is 12% K^{-1}, which is comparable to the spread in CMIP6 models of 14% K^{-1}. Relatedly, the spread in GMS response in AMIP models is 13% K^{-1} and the spread in CMIP6 models is 14% K^{-1}. This indicates that the atmosphere has a key role in the response of the WC to warming. Still, the strong role of the atmosphere does not preclude a role of the ocean since the spread from each component separately need not sum to the total spread of the coupled system. In addition, the ascent and descent regions of the WC are not in exactly the same location in each GCM which may complicate the comparison of CMIP6 simulations with the AMIP simulations in which the SST response is imposed the same way in all models.

The role of radiation is substantial in both CMIP6 and AMIP models. In the CMIP6 models, there is a multimodel mean weakening of the WC of 12% K^{-1} with a multimodel mean contribution of 7% K^{-1} from radiation. In the AMIP models, there is a multimodel mean weakening of the WC of 12% K^{-1} with a multmodel mean contribution of 5% K^{-1} from radiation. The radiation contribution is always the same sign as the GMS contribution; that is, contributing a weakening. Further, the decomposition of the radiation contribution (Figures 1c,d) indicates a strong role of WC-linked changes in radiation across CMIP6 and AMIP models. We hypothesize that cloud and/or water-vapor radiative feedbacks are amplifying the WC and GMS responses in CMIP6 and AMIP models, and such

feedbacks have been previously found to affect the WC strength (e.g., Peters and Bretherton (2005)).

The GMS response to warming involves changes in the vertical profiles of MSE and vertical velocity. Both the vertical profile of MSE and the shape of the vertical velocity profile contribute to the spread across CMIP6 and AMIP simulations in GMS response. They are both sensitive to convective entrainment which is an uncertain and parameterized process in GCMs. Therefore, we evaluate the role of entrainment in setting GMS and WC strength in an idealized GCM. To do so, we modify the simplified Betts Miller convection scheme of Frierson (2007) to include a simple representation of entrainment. We find that horizontal MSE advection plays an important role in the WC in some simulations, which is complicating because we do not have a theory for the relationship between entrainment and horizontal advection. To address this, we define a boundary GMS which approximately includes the role of horizontal MSE advection while not involving horizontal velocities and horizontal MSE gradients. Rather, the boundary GMS involves vertical advection of MSE profiles averaged over the boundary of each of the ascent and descent regions. We find that the WC weakens with warming, but less so at higher entrainment rates. This is consistent with increases in boundary GMS that get weaker with increasing entrainment. The effect of increased entrainment on GMS response can be understood through the fact that entrainment tends to make the atmosphere less stable in terms of the vertical profile of MSE, and it does so to a greater extent in the warmer climate. However, entrainment also affects the shape of the vertical-velocity profile, and this tends to weaken the effect of entrainment on GMS. The results from the idealized GCM provide a demonstration of a causal linkage between an imposed change in thermal stratification that affects the GMS and WC strength in a way that is consistent with the energetic analysis.

We conclude that the atmosphere plays a key role in setting the spread in WC response to warming, especially changes in GMS and cloud-radiative feedbacks. Convective entrainment influences GMS response and thus the WC response. Meanwhile, the spread in GMS response across CMIP6 and AMIP models is more from variations in vertical velocity profiles than variations in MSE profiles, and thus it seems unlikely that differences in representation of entrainment are the dominant source of spread across CMIP6 and AMIP models. Rather, other influences on vertical velocity profiles are likely a major cause of the substantial spread in WC response in GCMs and should be investigated in future work.

Table 1. CMIP6 and AMIP models, variant IDs, and citations.

Center	Model	CMIP6	AMIP	Citation
CSIRO-ARCCSS	ACCESS-CM2	r1i1p1f1		Dix et al. (2019)
AWI	AWI-CM-1-1-MR	r1i1p1f1		Semmler et al. (2019)
BCC	BCC-CSM2-MR	r1i1p1f1	r1i1p1f1	Wu et al. (2019); Xin et al. (2019)
CCCma	CanESM5	r1i1p1f1	r1i1p2f1	Swart et al. (2019); Cole et al. (2019)
NCAR	CESM2	r4i1p1f1	r1i1p1f1	Danabasoglu (2019)
CMCC	CMCC-CM2-SR5	r1i1p1f1		Lovato and Peano (2020)
CNRM-CERFACS	CNRM-CM6-1	r1i1p1f2	r1i1p1f2	Voldoire (2018)
EC-Earth-Consortium	EC-Earth3	r1i1p1f1		Consortium (2019)
CAS	FGOALS-f3-L	r1i1p1f1		Yu (2019)
FIO-QLNM	FIO-ESM-2-0	r1i1p1f1		Song et al. (2019)
NOAA-GFDL	GFDL-ESM4	r1i1p1f1		Krasting et al. (2018); John et al. (2018)
MOHC	HadGEM3-GC31-LL	r1i1p1f3	r5i1p1f3	Ridley et al. (2019); Webb (2019); Good (2020)
INM	INM-CM5-0	r1i1p1f1		Volodin et al. (2019)
IPSL	IPSL-CM6A-LR	r1i1p1f1	r1i1f1p1	Boucher et al. (2018)
NIMS-KMA	KACE-1-0-G	r1i1p1f1		Byun et al. (2019)
MIROC	MIROC6	r1i1p1f1	r1i1f1p1	Ogura et al. (2019); Tatebe and Watanabe (2018); Shiogama et al. (2019)
MPI-M	MPI-ESM1-2-LR	r1i1p1f1		Wieners et al. (2019)
MRI	MRI-ESM2-0	r1i1p1f1	r1i1f1p1	Yukimoto et al. (2019)
NUIST	NESM3	r1i1p1f1		Cao (2019)
NCC	NorESM2-MM	r1i1p1f1		Bentsen et al. (2019)
AS-RCEC	TaiESM	r1i1p1f1	r1i1f1p1	Lee and Liang (2019); Shiu et al. (2021)

Appendix A The entraining simplified Betts-Miller convection scheme

The SBM convection scheme of Frierson (2007) relaxes temperature profiles to a moist adiabat. Here, the scheme is modified such that temperature profiles are relaxed to a that of an *entraining* plume. The target humidity profile is calculated as in the original scheme using the target temperature profile (based on the entraining plume) and a reference relative humidity of 70%. The entrainment rate, ϵ, varies inversely with height and is given by $\epsilon = \frac{\hat{\epsilon}}{z}$, where $\hat{\epsilon}$ is a non-dimensional entrainment parameter and z is height. The convection scheme represents an ensemble of clouds, each of which detrains at a different level, which is crudely represented by the inverse relationship with z. The temperature lapse rate is assumed to be dry-adiabatic below the lifted condensation level (LCL). Above the LCL,

$$\frac{\partial h_s}{\partial z} = -\epsilon \left(h_s - h_e\right), \tag{A1}$$

where $h_s = c_p T + gz + Lr_s$ is the saturation MSE, r_s is the saturation mixing ratio, and h_e is the environmental MSE. Here we use the GCM's gridbox MSE to represent the environmental MSE. Using the definition of h_s gives

$$c_p \frac{dT}{dz} + g + L\frac{dr_s}{dz} = -\epsilon \left(h_s - h_e\right). \tag{A2}$$

Using $r_s = r_s(T, p)$ and applying the hydrostatic equation gives

$$c_p \frac{dT}{dz} + g + L\frac{\partial r_s}{\partial T}\frac{dT}{dz} - L\rho g \frac{\partial r_s}{\partial p} = -\epsilon \left(h_s - h_e\right). \tag{A3}$$

Next, group like terms to give

$$(c_p + L\frac{\partial r_s}{\partial T})\frac{\partial T}{\partial z} + g - L\rho g \frac{\partial r_s}{\partial p} = -\epsilon \left(h_s - h_e\right). \tag{A4}$$

Rearranging to solve for $\frac{\partial T}{\partial z}$ gives

$$\frac{\partial T}{\partial z} = \frac{-\epsilon \left(h_s - h_e\right) - g + L\rho g \frac{\partial r_s}{\partial p}}{c_p + L\frac{\partial r_s}{\partial T}}. \tag{A5}$$

Following the original scheme, we approximate the partial derivatives of r_s with respect to pressure and temperature as $\partial r_s/\partial p = -r_s/p$ and $\partial r_s/\partial T = Lr_s/(R_v T^2)$, respectively, where R_v is the gas constant for water vapor. Substituting these two expressions into Equation A5 and applying the ideal gas law gives

$$\frac{\partial T}{\partial z} = \frac{-\epsilon \left(h_s - h_e\right) - g(1 + \frac{Lr_s}{RT})}{c_p + \frac{L^2 r_s}{R_v T^2}}. \tag{A6}$$

Using the hydrostatic equation and the ideal gas law gives the lapse rate of the entraining plume above the LCL

$$\frac{\partial T}{\partial \ln p} = \frac{\frac{RT}{gc_p}\epsilon \left(h_s - h_e\right) + \frac{RT}{c_p} + \frac{Lr_s}{c_p}}{1 + \frac{L^2 r_s}{c_p R_v T^2}}. \tag{A7}$$

Notice that the temperature profile for the entraining plume reduces to a moist adiabat when $\epsilon = 0$.

Open Research

We acknowledge the World Climate Research Programme, which, through its Working Group on Coupled Modelling, coordinated and promoted CMIP6. We thank the climate modeling groups for producing and making available their model output, the Earth System Grid Federation (ESGF) for archiving the data and providing access, and the

multiple funding agencies who support CMIP6 and ESGF. Each model and the variant ID of the simulations used is listed in Table 1. The modified version of the GFDL idealized moist spectral atmospheric model and the analysis scripts used for this work is available on Zenodo at https://sandbox.zenodo.org/record/1075519.

Acknowledgments

We thank Robert Jnglin Wills, Tristan Abbott, and Janni Yuval for help in setting up the idealized GCM simulations. We thank Larissa Back, Tim Cronin, and Adam Schlosser for useful feedback. This research was supported by NSF-AGS 1749986.

References

Bentsen, M., Oliviè, D. J. L., Seland, o., Toniazzo, T., Gjermundsen, A., & et al. (2019). NCC NorESM2-MM model output prepared for CMIP6 CMIP historical and ScenarioMIP ssp585. Earth System Grid Federation. (Version: 20191108 [dataset]) doi: https://doi.org/10.22033/ESGF/CMIP6.506

Boucher, O., Denvil, S., Levavasseur, G., Cozic, A., Caubel, A., Foujols, M.-A., & et al. (2018). IPSL IPSL-CM6A-LR model output prepared for CMIP6 CMIP historical, ScenarioMIP ssp585, CMIP amip, and CFMIP amip-future4K. Earth System Grid Federation. (Version: 20180803 [dataset]) doi: https://doi.org/10.22033/ESGF/CMIP6.1521

Byun, Y.-H., Lim, Y.-J., Shim, S., Sung, H. M., Sun, M., Kim, J., & et al. (2019). NIMS-KMA KACE1.0-G model output prepared for CMIP6 CMIP historical ScenarioMIP ssp585. Earth System Grid Federation. (Version: 20190920 [dataset]) doi: https://doi.org/10.22033/ESGF/CMIP6.2241

Cao, J. (2019). NUIST NESMv3 model output prepared for CMIP6 CMIP historical and ScenarioMIP ssp585. Earth System Grid Federation. (Version: 20190728 [dataset]) doi: https://doi.org/10.22033/ESGF/CMIP6.2021

Chou, C., Wu, T.-C., & Tan, P.-H. (2013). Changes in gross moist stability in the tropics under global warming. *Climate Dynamics*, *41*(9-10), 2481–2496. doi: https://doi.org/10.1007/s00382-013-1703-2

Clement, A. C., Seager, R., Cane, M. A., & Zebiak, S. E. (1996). An ocean dynamical thermostat. *Journal of Climate*, *9*(9), 2190–2196. doi: https://doi.org/10.1175/1520-0442(1996)009⟨2190:AODT⟩2.0.CO;2

Cole, J. N., von Salzen, K., Swart, N. C., Kharin, V. V., Lazare, M., Scinocca, J. F., & et al. (2019). CCCma CanESM5 model output prepared for CMIP6 CFMIP amip-future4K. Earth System Grid Federation. (Version: 20190429 [dataset]) doi: https://doi.org/10.22033/ESGF/CMIP6.1301

Consortium, E.-E. (2019). EC-Earth-Consortium EC-Earth3 model output prepared for CMIP6 CMIP historical and ScenarioMIP ssp585. Earth System Grid Federation. (Version: 20200310 [dataset]) doi: https://doi.org/10.22033/ESGF/CMIP6.181

Danabasoglu, G. (2019). NCAR CESM2 model output prepared for CMIP6 CMIP historical, ScenarioMIP ssp585, CMIP amip, and CFMIP amip-future4K. Earth System Grid Federation. (Version: 20190401 [dataset]) doi: https://doi.org/10.22033/ESGF/CMIP6.2181

DiNezio, P. N., Clement, A. C., Vecchi, G. A., Soden, B. J., & Kirtman, B. P. (2009). Climate response of the equatorial pacific to global warming. *Journal of Climate*, *22*(18), 4873–4892. doi: https://doi.org/10.1175/2009JCLI2982.1

Dix, M., Bi, D., Dobrohotoff, P., Fiedler, R., Harman, I., Law, R., & et al. (2019). CSIRO-ARCCSS ACCESS-CM2 model output prepared for CMIP6 CMIP historical and ScenarioMIP ssp585. Earth System Grid Federation. (Version: 20210317 [dataset]) doi: https://doi.org/10.22033/ESGF/CMIP6.2281

Frierson, D. M. W. (2007). The dynamics of idealized convection schemes and their

effect on the zonally averaged Tropical circulation. *Journal of the Atmospheric Sciences*, *64*(6), 1959–1976. doi: https://doi.org/10.1175/JAS3935.1

Frierson, D. M. W., Held, I. M., & Zurita-Gotor, P. (2006). A gray-radiation aquaplanet moist GCM. Part I: Static stability and eddy scale. *Journal of the Atmospheric Sciences*, *63*(10), 2548–2566. doi: https://doi.org/10.1175/JAS3753.1

Good, P. (2020). MOHC HadGEM3-GC31-LL model output prepared for CMIP6 ScenarioMIP ssp585. Earth System Grid Federation. (Version: 20200114 [dataset]) doi: https://doi.org/10.22033/ESGF/CMIP6.10845

Heede, U. K., & Fedorov, A. V. (2021). Eastern equatorial Pacific warming delayed by aerosols and thermostat response to CO2 increase. *Nature Climate Change*, *11*(8), 696–703. doi: https://doi.org/10.1038/s41558-021-01101-x

Held, I. M., & Soden, B. J. (2006). Robust responses of the hydrological cycle to global warming. *Journal of Climate*, *19*(21), 5686–5699. doi: https://doi.org/10.1175/JCLI3990.1

Held, I. M., Zhao, M., & Wyman, B. (2007). Dynamic radiative-convective equilibria using GCM column physics. *Journal of the Atmospheric Sciences*, *64*(1), 228–238. doi: https://doi.org/10.1175/JAS3825.11

Inoue, K., Biasutti, M., & Fridlind, A. M. (2021). Evidence that horizontal moisture advection regulates the ubiquitous amplification of rainfall variability over Tropical oceans. *Journal of the Atmospheric Sciences*, *78*(2), 529–547. doi: https://doi.org/10.1175/JAS-D-20-0201.1

John, J. G., Blanton, C., McHugh, C., Radhakrishnan, A., Rand, K., Vahlenkamp, H., & et al. (2018). NOAA-GFDL GFDL-ESM4 model output prepared for CMIP6 ScenarioMIP ssp585. Earth System Grid Federation. (Version: 20180701 [dataset]) doi: https://doi.org/10.22033/ESGF/CMIP6.1407

Keil, P., Schmidt, H., Stevens, B., & Bao, J. (2021). Variations of tropical lapse rates in climate models and their implications for upper tropospheric warming. *Journal of Climate*, 1–50. doi: https://doi.org/10.1175/JCLI-D-21-0196.1

Knutson, T. R., & Manabe, S. (1995). Time-mean response over the Tropical Pacific to increased CO_2 in a coupled ocean-atmosphere model. *Journal of Climate*, *8*(9), 2181–2199. doi: https://doi.org/10.1175/1520-0442(1995)008⟨2181:TMROTT⟩2.0.CO;2

Krasting, J. P., John, J. G., Blanton, C., McHugh, C., Nikonov, S., Radhakrishnan, A., & et al. (2018). NOAA-GFDL GFDL-ESM4 model output prepared for CMIP6 CMIP historical. Earth System Grid Federation. (Version: 20190726 [dataset]) doi: https://doi.org/10.22033/ESGF/CMIP6.1407

Lee, W.-L., & Liang, H.-C. (2019). AS-RCEC TaiESM1.0 model output prepared for CMIP6 CMIP historical, CMIP, ScenarioMIP ssp585, and CMIP amip. Earth System Grid Federation. (Version: 20200817 [dataset]) doi: https://doi.org/10.22033/ESGF/CMIP6.9684

Lovato, T., & Peano, D. (2020). CMCC CMCC-CM2-SR5 model output prepared for CMIP6 CMIP historical and ScenarioMIP ssp585. Earth System Grid Federation. (Version: 20200622 [dataset]) doi: https://doi.org/10.22033/ESGF/CMIP6.1362

Ma, J., Xie, S.-P., & Kosaka, Y. (2012). Mechanisms for tropical tropospheric circulation change in response to global warming. *Journal of Climate*, *25*(8), 2979–2994. doi: https://doi.org/10.1175/JCLI-D-11-00048.1

Merlis, T. M. (2015). Direct weakening of tropical circulations from masked CO_2 radiative forcing. *Proceedings of the National Academy of Sciences*, *112*(43), 13167–13171. doi: https://doi.org/10.1073/pnas.1508268112

Merlis, T. M., & Schneider, T. (2011). Changes in zonal surface temperature gradients and Walker circulations in a wide range of climates. *Journal of Climate*, *24*(17), 4757–4768. doi: https://doi.org/10.1175/2011JCLI4042.1

Merlis, T. M., Schneider, T., Bordoni, S., & Eisenman, I. (2013). Hadley circula-

tion response to orbital precession. Part II: Subtropical continent. *Journal of Climate*, *26*(3), 754–771. doi: https://doi.org/10.1175/JCLI-D-12-00149.1

Miyawaki, O., Tan, Z., Shaw, T. A., & Jansen, M. F. (2020). Quantifying key mechanisms that contribute to the deviation of the tropical warming profile from a moist adiabat. *Geophysical Research Letters*, *47*(20). doi: https://doi.org/10.1029/2020GL089136

Neelin, J. D., & Held, I. M. (1987). Modeling tropical convergence based on the moist static energy budget. *Monthly Weather Review*, *115*(1), 3–12. doi: https://doi.org/10.1175/1520-0493(1987)115⟨0003:MTCBOT⟩2.0.CO;2

O'Gorman, P. A., & Schneider, T. (2008). The hydrological cycle over a wide range of climates simulated with an idealized GCM. *Journal of Climate*, *21*(15), 3815–3832. doi: https://doi.org/10.1175/2007JCLI2065.1

Ogura, T., Watanabe, M., & Hirota, N. (2019). MIROC MIROC6 model output prepared for CMIP6 CFMIP amip-future4K. Earth System Grid Federation. (Version: 20190705 [dataset]) doi: https://doi.org/10.22033/ESGF/CMIP6.885

Peters, M. E., & Bretherton, C. S. (2005). A simplified model of the Walker circulation with an interactive ocean mixed layer and cloud-radiative feedbacks. *Journal of Climate*, *18*(20), 4216–4234. doi: 10.1175/JCLI3534.1

Raymond, D. J., Sessions, S. L., Sobel, A. H., & Fuchs, Z. (2009). The mechanics of gross moist stability. *Journal of Advances in Modeling Earth Systems*, *1*(3), n/a–n/a. doi: https://doi.org/10.3894/JAMES.2009.1.9

Ridley, J., Menary, M., Kuhlbrodt, T., Andrews, M., & Andrews, T. (2019). MOHC HadGEM3-GC31-LL model output prepared for CMIP6 CMIP amip. Earth System Grid Federation. (Version: 20191001 [dataset]) doi: https://doi.org/10.22033/ESGF/CMIP6.419

Romps, D. M. (2010). A direct measure of entrainment. *Journal of the Atmospheric Sciences*, *67*(6), 1908–1927. doi: https://doi.org/10.1175/2010JAS3371.1

Semmler, T., Danilov, S., Rackow, T., Sidorenko, D., Barbi, D., Hegewald, J., & et al. (2019). AWI AWI-CM1.1MR model output prepared for CMIP6 CMIP historical and ScenarioMIP ssp585. Earth System Grid Federation. (Version: 20190529 [dataset]) doi: https://doi.org/10.22033/ESGF/CMIP6.359

Shiogama, H., Abe, M., & Tatebe, H. (2019). MIROC MIROC6 model output prepared for CMIP6 ScenarioMIP ssp585. Earth System Grid Federation. (Version: 20190627 [dataset]) doi: https://doi.org/10.22033/ESGF/CMIP6.898

Shiu, C.-J., Lee, W.-L., & Hsu, H.-H. (2021). AS-RCEC TaiESM1.0 model output prepared for CMIP6 CFMIP amip-future4K. Earth System Grid Federation. (Version: 20210820 [dataset]) doi: https://doi.org/10.22033/ESGF/CMIP6.9683

Singh, M. S., & Neogi, S. (2022). On the interaction between moist convection and large-scale ascent in the tropics. *Journal of Climate*, *35*(14), 4417–4435. doi: https://doi.org/10.1175/JCLI-D-21-0717.1

Singh, M. S., & O'Gorman, P. A. (2012). Upward shift of the atmospheric general circulation under global warming: Theory and simulations. *Journal of Climate*, *25*(23), 8259–8276. doi: https://doi.org/10.1175/JCLI-D-11-00699.1

Singh, M. S., & O'Gorman, P. A. (2013). Influence of entrainment on the thermal stratification in simulations of radiative-convective equilibrium. *Geophysical Research Letters*, *40*(16), 4398–4403. doi: https://doi.org/10.1002/grl.50796

Sohn, B.-J., Lee, S., Chung, E.-S., & Song, H.-J. (2016). The role of the dry static stability for the recent change in the Pacific Walker circulation. *Journal of Climate*, *29*(8), 2765–2779. doi: https://doi.org/10.1175/JCLI-D-15-0374.1

Song, Z., Qiao, F., Bao, Y., Shu, Q., Song, Y., & Yang, X. (2019). FIO-QLNM FIO-ESM2.0 model output prepared for CMIP6 CMIP historical and ScenarioMIP ssp585. Earth System Grid Federation. (Version: 20191226 [dataset]) doi: https://doi.org/10.22033/ESGF/CMIP6.9047

Su, H., & Neelin, J. D. (2002). Teleconnection mechanisms for tropical Pacific de-

scent anomalies during El Niño. *Journal of the Atmospheric Sciences*, *59*(18), 2694–2712. doi: https://doi.org/10.1175/1520-0469(2002)059⟨2694:TMFTPD⟩2.0.CO;2

Swart, N. C., Cole, J. N., Kharin, V. V., Lazare, M., Scinocca, J. F., Gillett, N. P., & et al. (2019). CCCma CanESM5 model output prepared for CMIP6 CMIP historical, ScenarioMIP ssp585, and CMIP amip. Earth System Grid Federation. (Version: 20190429 [dataset]) doi: https://doi.org/10.22033/ESGF/CMIP6.10205

Tatebe, H., & Watanabe, M. (2018). MIROC MIROC6 model output prepared for CMIP6 CMIP historical and CMIP amip. Earth System Grid Federation. (Version: 20181212 [dataset]) doi: https://doi.org/10.22033/ESGF/CMIP6.881

Trenberth, K. E., & Stepaniak, D. P. (2003). Seamless poleward atmospheric energy transports and implications for the Hadley circulation. *Journal of Climate*, *16*(22), 3706–3722. doi: https://doi.org/10.1175/1520-0442(2003)016⟨3706:SPAETA⟩2.0.CO;2

Vecchi, G. A., & Soden, B. J. (2007). Global warming and the weakening of the tropical circulation. *Journal of Climate*, *20*(17), 4316–4340. doi: https://doi.org/10.1175/JCLI4258.1

Vecchi, G. A., Soden, B. J., Wittenberg, A. T., Held, I. M., Leetmaa, A., & Harrison, M. J. (2006). Weakening of tropical Pacific atmospheric circulation due to anthropogenic forcing. *Nature*, *441*(7089), 73–76. doi: https://doi.org/10.1038/nature04744

Voldoire, A. (2018). CNRM-CERFACS CNRM-CM6-1 model output prepared for CMIP6 CMIP historical, ScenarioMIP ssp585, CMIP amip and CFMIP amip-future4K. Earth System Grid Federation. (Version: 20181203 [dataset]) doi: https://doi.org/10.22033/ESGF/CMIP6.1374

Volodin, E., Mortikov, E., Gritsun, A., Lykossov, V., Galin, V., Diansky, N., & et al. (2019). INM INM-CM5-0 model output prepared for CMIP6 CMIP historical and ScenarioMIP ssp585. Earth System Grid Federation. (Version: 20190610 [dataset]) doi: https://doi.org/10.22033/ESGF/CMIP6.1423

Webb, M. (2019). MOHC HadGEM3-GC31-LL model output prepared for CMIP6 CMIP historical and CFMIP amip-future4K. Earth System Grid Federation. (Version: 20191216 [dataset]) doi: https://doi.org/10.22033/ESGF/CMIP6.435

Wieners, K.-H., Giorgetta, M., Jungclaus, J., Reick, C., Esch, M., Bittner, M., & et al. (2019). MPI-M MPI-ESM1.2-LR model output prepared for CMIP6 CMIP historical and ScenarioMIP ssp585. Earth System Grid Federation. (Version: 20190710 [dataset]) doi: 10.22033/ESGF/CMIP6.6705

Wills, R. C., Levine, X. J., & Schneider, T. (2017). Local energetic constraints on Walker circulation strength. *Journal of the Atmospheric Sciences*, *74*(6), 1907–1922. doi: https://doi.org/10.1175/JAS-D-16-0219.1

Wu, T., Chu, M., Dong, M., Fang, Y., Jie, W., Li, J., & et al. (2019). BCC BCC-CSM2MR model output prepared for CMIP6 CMIP historical, CMIP amip and CFMIP amip-future4K. Earth System Grid Federation. (Version: 20200720 [dataset]) doi: https://doi.org/10.22033/ESGF/CMIP6.2856

Xin, X., Wu, T., Shi, X., Zhang, F., Li, J., Chu, M., & et al. (2019). BCC BCC-CSM2MR model output prepared for CMIP6 ScenarioMIP ssp585. Earth System Grid Federation. (Version: 20190314 [dataset]) doi: https://doi.org/10.22033/ESGF/CMIP6.1725

Yu, Y. (2019). CAS FGOALS-f3-L model output prepared for CMIP6 CMIP historical and ScenarioMIP ssp585. Earth System Grid Federation. (Version: 20191013 [dataset]) doi: https://doi.org/10.22033/ESGF/CMIP6.1782

Yukimoto, S., Koshiro, T., Kawai, H., Oshima, N., Yoshida, K., Urakawa, S., & et al. (2019). MRI MRI-ESM2.0 model output prepared for CMIP6 CMIP historical, ScenarioMIP ssp585, CMIP amip, and CFMIP amip-

future4K. Earth System Grid Federation. (Version: 20190625 [dataset]) doi: https://doi.org/10.22033/ESGF/CMIP6.623